

Article

Experimental Study and Damage Model on the Seismic Behavior of Reinforced Concrete L-Shaped Columns under Combined Torsion

Deyi Xu ¹, Yang Yang ² and Zongping Chen ^{1,3,*}

¹ College of Civil Engineering and Architecture, Guangxi University, Nanning 530004, China; xudeyi195@st.gxu.edu.cn

² Department of Project Management; Hunan Vocational College of Engineering, Changsha 410151, China; brian622795@gmail.com

³ Key Laboratory of Disaster Prevention and Structure Safety of Chinese Ministry of Education, Guangxi University, Nanning 530004, China

* Correspondence: zpchen@gxu.edu.cn; Tel.: +86-13878806048

Received: 23 August 2020; Accepted: 27 September 2020; Published: 8 October 2020



Abstract: Due to the advantage of saving indoor space, a special-shaped column frame attracted more attention of the engineers and researchers. This paper presented a quasi-static cyclic loading experiment of six specimens of reinforced concrete (RC) L-shaped columns under compression-flexure-shear-torsion combined loadings to investigate the effect in the ratio of torsion to moment (T/M) and axial compression ratio (n) on their seismic performance. The results showed that the failure modes of L-shaped specimens included bending failure, bending-torsion failure, and torsion-shear failure with the hysteretic curves exhibiting S shape. With the increase of T/M ratio, cracks on the flange developed more fully, and the height of plastic hinge decreased and torsion bearing capacity improved. Besides, as the T/M ratio increased the twist ductility increased, while displacement ductility decreased. On the other hand, with a higher axial compression ratio, torsion bearing capacity and bending stiffness were both increased. Moreover, the equivalent viscous damping coefficient of bending and torsion were 0.08~0.28 and 0.13~0.23, respectively. The average inter-story drift ratio met the requirements of the Chinese standard. Finally, two modified models were proposed to predict the progression of damage for the L-shaped column under combined loading including torsion.

Keywords: reinforced concrete; L-shaped column; compression-flexure-shear-torsion; combined action; seismic behavior

1. Introduction

Compared with traditional rectangle columns, the special-shaped (L, T, +) columns have advantages of refraining from the wall, increasing the interior space, and improving the flexibility in the use of architectural space, due to the limb of the special-shaped column as thick as the wall. Therefore, it is favored deeply by buyers and architects [1,2]. Figure 1 shows practical engineering projects in which special-shaped columns have been employed.

In the past few decades, many experimental and analytical studies have been carried out to study the mechanical property of special-shaped columns [3–9]. In addition, great efforts have been taken to reveal the seismic performance of RC special-shaped columns under axial force and bending load or bending and shear force. Based on the tests of 12 RC special-shaped columns, Cao et al. [10] found that concealed columns can improve the bearing capacity significantly. Liu et al. [11] carried out a shaking table test of a 9-story RC special-shaped frame model with the transfer story. The test showed that

this structure can be used in the region of earthquake intensity. Cui et al. [12] studied the effects of the horizontal loading directions (0° , 45° , 90° , and 135°) on the seismic performance of RC Z-shaped columns. Test results show that four types of failure modes can be observed including shear-bending failure, bending failure, shear failure, and shear-compression failure. Li B and Pham T. P [13] carried out the investigation on 10 RC columns with L-shaped sections, which were subjected to simulated seismic loadings. All specimens exhibit a significant pinching and the longitudinal reinforcement yielded before the maximum shear force reached.

Cracks and damages observed from RC special-shaped columns after earthquake indicate that multi-directional earthquake motions and movement of joints could result in failure due to torsional oscillations. In addition, different from RC rectangular columns, shear center and mass center of RC special-shaped columns do not locate in the same position. Thus, the torsion effect exists due to the effect of the horizontal earthquake force. It is necessary to investigate the seismic performance of RC special-shaped columns subjected to the combined loading including axial compression, shear, moment, and torsion.

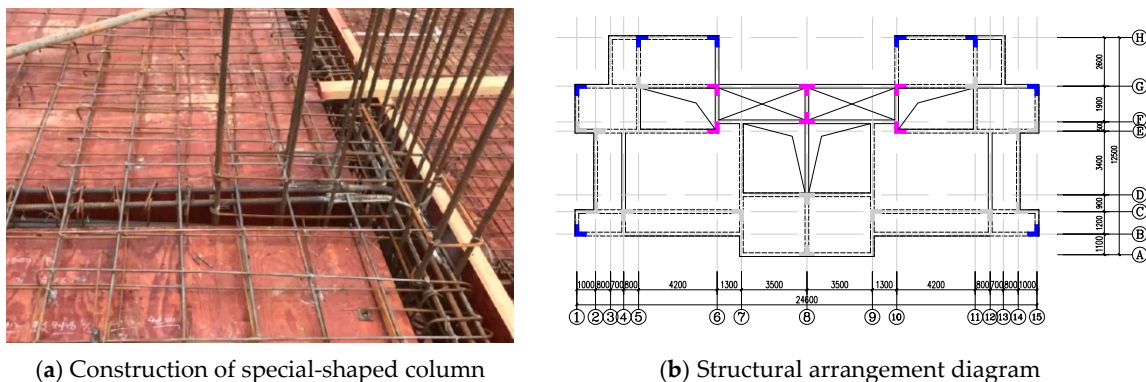


Figure 1. The special-shaped columns used in the practical engineering.

In previous research, it was shown that the ratio of the torsion moment to the bending moment at the bottom section (T/M) had a significant effect on seismic performance. Nie et al. [14,15] studied the seismic performance of concrete-filled circular/rectangular steel tube columns under combined torsion. They found that the bending capacity decreased with increasing of T/M ratio, while the torsional capacity increased. Other researchers, such as Otsuka et al. [16], Hsu et al. [17,18], Tirasit and Kawashima [19] also found the same interaction effect between torsion and flexure. Li Q and Belarbi A [20,21] conducted research on the 7 RC bridge columns under compression, bending, shear, and torsion. They pointed out that the location and length of the damage zone moved upward from the base of the column as the T/M ratio increased, with the failure mode and deformation characteristics changed. Investigation showed that the form of structures can also affect its seismic performance. Belarbi et al. [22] and Prakash et al. [23] conduct experiments with a series of specimens under pure torsion, pure flexure, and combined torsions. These results indicated that there was a significant change in the failure mode and deformation characteristics not only due to T/M ratio, but also to the construction and reinforcement. Wang et al. [24] found that the decreasing of stirrup spacing can improve the torsional strength of columns, but it had little influence on the bending performances, which is in accordance with the finding by Deng et al. [25]. Anumolu et al. [26] developed a three-dimensional model of an HC-SCS column under combined torsion. Moreover, they also developed a simplified equation to predict the torsion strength. Mullapudi T R S [27] put forward a three-dimensional model of RC members subjected to combined torsion. They used the model to assess the seismic performance, which also matched the experimental results well. Prakash [28] proposed damage index models permitting decoupling these combined loadings including bending and torsion. The models could evaluate the interaction between flexural and torsional damage models according to the progression of damage. Through performance-based evaluation, Belarbi [29] proposed a damage model for the

square and circular column under bending, shear, axial compression, and torsion. Li [21] conducted experimental and analytical studies on four square RC column under torsion combined with axial compression, flexure, and shear. Based on the observation of the experiment, a unified equivalent damage model considering the T/M ratio was proposed to couple the flexural and torsional actions.

The previous literature showed that there were few studies on the seismic behavior of RC L-shaped columns (RCL) under combined loadings including compression, flexure, shear, and torsion. Besides, the knowledge of the interaction between flexural and torsional in the behavior of the RC L-shaped columns is also limited. To expand the application of RC special-shaped columns, six RC L-shaped columns with different T/M ratio and axial compression ratios ($n = N/(f_{ck}A)$) were designed to conduct the low cycle reversed loading test. The effects of combined torsion on a hysteretic torsional and a flexural response, failure modes, carrying capacity, ductility characteristics, strength and stiffness degradation, energy dissipation, and interlayer displacement angle will be discussed. Two decoupled flexural and torsional damage index models were proposed to predict the progression of damage for the L-shaped column under combined loadings.

2. Experimental Section

2.1. Specimens Details

A total of six specimens with different T/M ratios (i.e., 0.00, 0.17, 0.28, 0.36) and axial compression ratios (i.e., 0.19, 0.23, 0.28) were designed for the cyclic loading test. The details for the specimens are shown in Figure 2. All specimens were identical to each other. The effective height was 1180 mm measured from the bottom of the column to the loading point. The height and thickness of the column limb were 360 and 120 mm, respectively. Both the longitudinal reinforcement and stirrup strain gauges were pasted at the middle height of the column. The concrete cover for all the specimens was 15 mm. The longitudinal reinforcement ratio and the transverse reinforcement ratio for the specimens were 1.36% and 0.94%, respectively. Longitudinal bars were 16 mm in diameter with yield strength $f_y = 418$ MPa and ultimate strength $f_u = 577$ MPa. Transverse reinforcement was 6 mm in diameter with yield strength $f_y = 340$ MPa and ultimate strength $f_u = 472$ MPa. All specimens were made of commercial concrete with the concrete strength $f_{cu} = 30.4$ MPa.

2.2. Test Setup and Procedure

Test setup offering combined compression, bending moment, shear, and torsion with two electro-hydraulic servo actuators is shown in Figure 3. The actuators were fixed by four steel reaction screws and two girders. Axial load was applied at the top of the column with an axial loading arrangement, which consisted of a hydraulic jack, spherical hinge, roller, loading beam, and reaction frame. Then, the combined bending moment and torsion were generated by two actuators. Different T/M ratios were imposed by applying different ratios of force and displacement in the two actuators. The horizontal displacements of specimens were measured by displacement sensors installed in electro-hydraulic servo actuators. The load parameters of each specimen are presented in Table 1.

The loading process was mixed-loading pattern including load-controlled pattern and displacement-controlled pattern. During the load-controlled stage, loading amplitude was conducted in single cycle. When the specimen first yielded, the loading-controlled phase was transferred into the displacement-controlled phase. The horizontal displacement corresponding to the first yield point was named yield displacement Δ_y , which was taken as the cyclic displacement times for loading amplitude. In the displacement controlled phase, cyclic lateral loading was quasi-statically applied to the top beam according to the displacement-controlled pattern shown in Figure 4. Each displacement amplitude was conducted in three cycles to measurement the indication of strength and stiffness degradation characteristics. The test terminated when the lateral load resistance deteriorated to 85% of the maximum measured lateral load.

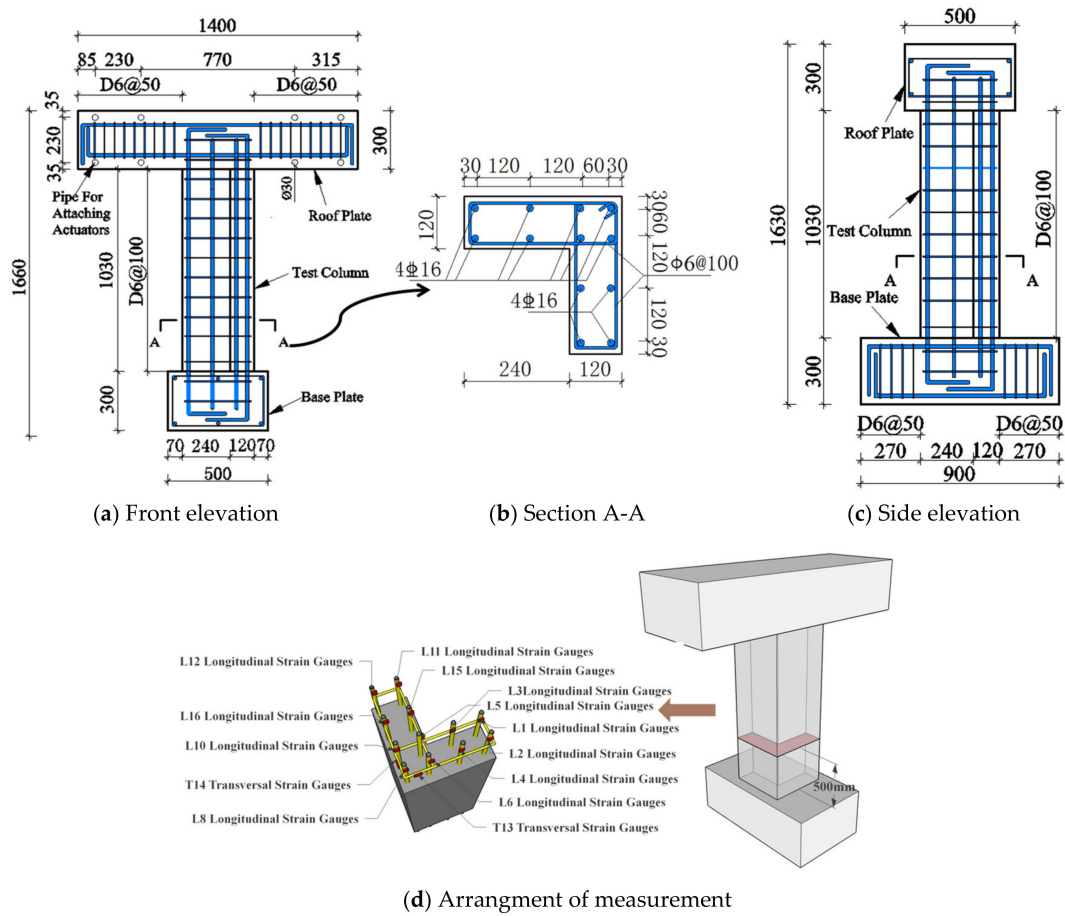


Figure 2. Detailed design of specimens (unit: mm).

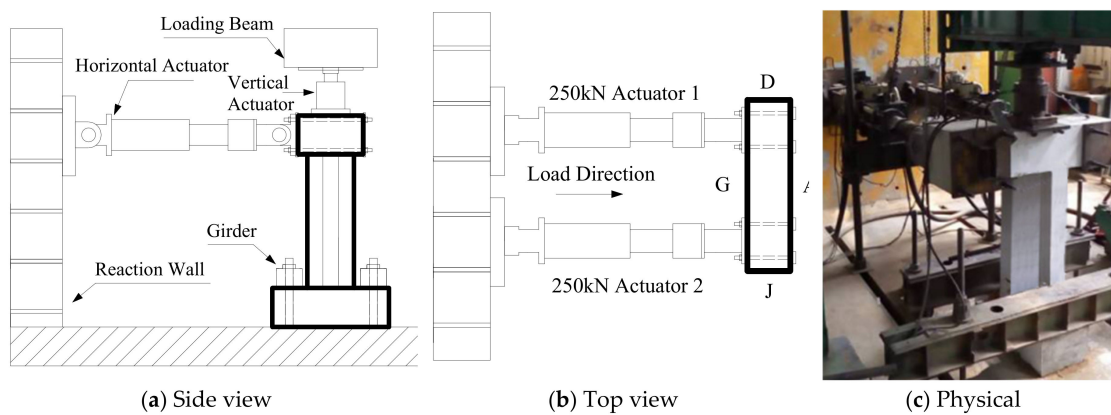


Figure 3. Test setup.

Table 1. Load parameters of specimens.

Specimen No.	Axial Compression Ratio	T/M Ratio
RCL-1	0.23	0.36
RCL-2	0.23	0.00
RCL-3	0.19	0.28
RCL-4	0.28	0.00
RCL-5	0.23	0.28
RCL-6	0.23	0.17

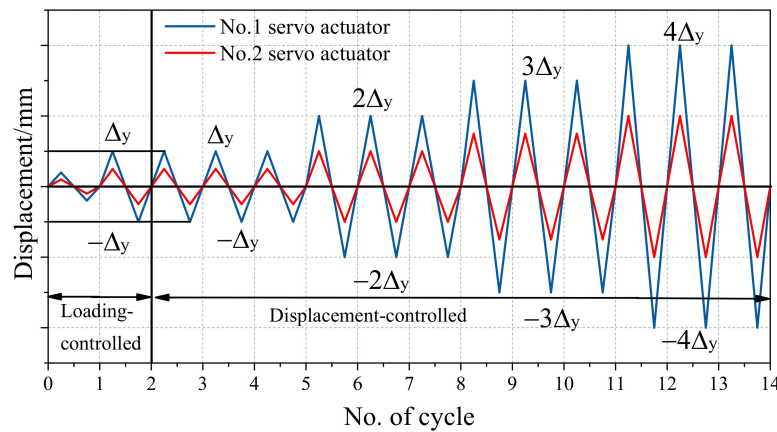


Figure 4. Loading history.

2.3. Loading Principle

The loading principle is shown in Figure 5. The force of actuator 2 (F_2) always has a constant proportion to the force of actuator 1 (F_1), and the proportional coefficient is defined as $\alpha = F_2/F_1$. Therefore, the bending moment and torsion moment at the bottom section of the specimen due to the two forces could be obtained as

$$M = (F_1 + F_2)H_e = (1 + \alpha)F_1H_e \tag{1}$$

$$T = (F_1 - F_2)L = (1 - \alpha)F_1L \tag{2}$$

H_e is the effective height of the column and L is the distance between the two concentrates. So the T/M ratio could be expressed as

$$r = T/M = \frac{(1 - \alpha)L}{(1 + \alpha)H_e} \tag{3}$$

From Equation (3) it can be seen that the load with an arbitrary T/M ratio could be applied to the specimen by changing the coefficient α . It is equal to the case under pure bending when the $T/M = 0$.

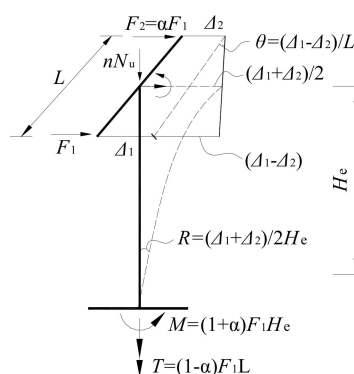


Figure 5. Loading principle.

3. Failure Modes

With the increase of the T/M ratio, failure modes of specimens exhibited bending failure, bending-torsion failure, and torsion-shear failure. Figure 6 shows crack patterns and failure modes for the specimens with the red cracks representing occurred when the specimen subjected the pull and blue cracks occurred when the specimen subjected the push. The L-shaped column consisted of

two column limbs where one, limb B, was parallel to the loading direction. The other one, limb A, was orthogonal to the loading direction.

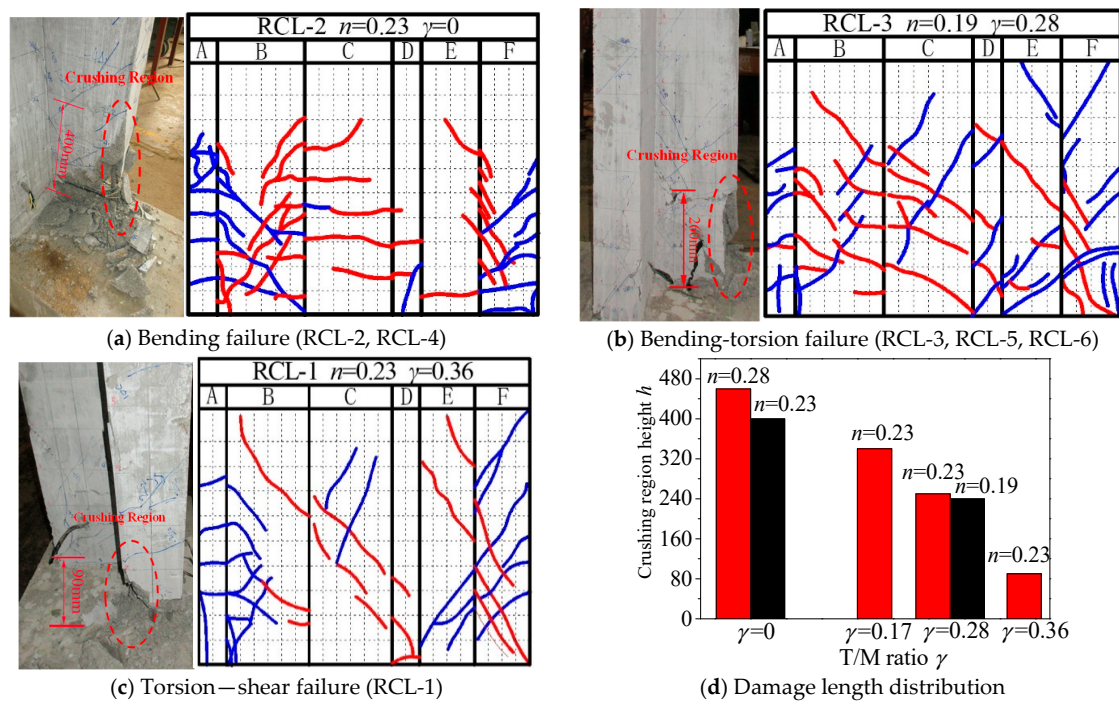


Figure 6. The failure pattern and cracks distribution.

3.1. Bending Failure

Specimens with T/M ratio = 0 exhibited a bending failure as shown in Figure 6a. A representative specimen (RCL-2) was selected to investigate the bending failure. When load reached 35 kN, the RCL-2 specimen initiated first horizontal flexural cracks on column limb B, which was parallel to the loading direction. As the displacement reached 12 mm, some horizontal flexural cracks appeared on column limb A which was vertical to the loading direction. At the same time, 45° diagonal cracks were observed and propagating to limb A on both sides of limb B. As the displacement reached to 18 mm, several vertical bond cracks occurred on the end corner of limb B. When displacement reached 30 mm, the vertical cracks on the column bottom were about 6~8 mm height with concrete spalling. The cracks were mainly horizontal cracks due to the bending moment. The specimen failed with damage zone height of 400 mm and the plastic hinge develops completely.

3.2. Bending-Torsion Failure

Specimens with T/M ratio = 0.17 and 0.28 presented a similar failure mode of bending-torsion failure, as shown in Figure 6b. A representative specimen (RCL-3) was selected to investigate the bending failure. During the load controlled procedure, at the 38 kN of lateral load, diagonal cracks of 20° increased on both sides of limbs A and B. In the displacement controlled procedure, horizontal cracks appeared at the bottom of limbs when displacement was 6 mm. Vertical bond cracks occurred at the corner of the column when displacement reached 12 mm. With the increase of horizontal displacement, the 45° diagonal cracks grew widened and deep at the inner side of the limb A. These cracks were mostly diagonal cracks between 20° and 30°. In the final stage, The specimen damaged with the concrete spalling and the plastic hinge height were observed between 240 and 300 mm.

3.3. Torsion-Shear Failure

Specimens with $T/M = 0.36$ exhibited the torsion-shear failure as shown in Figure 6c. A representative specimen of RCL-1 was selected. At 37 kN of lateral load, several X-shaped cracks (the inclination is about 45°) appeared on the middle of limb A. When displacement was 9 mm, the vertical bond cracks were detected on the bottom of limbs. With displacement increased, the cracks gradually propagated toward the top of the column, forming several X-shaped cracks. At the failure stage, the concrete on the bottom of the column limb crushed, and longitudinal bars were exposed. Specimens with torsion-shear failure were subjected to large torque. The crack angle on the column limb A and B mainly tended to 45° , the crushed area was about 90mm at the bottom with the plastic hinge developed.

3.4. The Height of Crushed Area

From the Figure 6d, with the increasing ratio of T/M (0.17, 0.28, 0.36), the height of the crushed concrete area declined by 35% and 77.5% compared to the specimens with the T/M ratio of 0.17. This is attributed to the change in failure mode. However, the specimen still had a favorable bearing ability. Further, the greater the axial compression ratio, the higher height of the crushed area.

4. Test Results Analysis

4.1. Hysteretic Behavior

The characteristic points (namely, the yielding load P_y and yielding displacement Δ_y , peak load P_u and peak displacement Δ_u , ultimate load P_f and ultimate displacement Δ_f) of the specimens, which were defined on the skeleton curve, were listed in Table 2. The yield load P_y corresponding to the yield displacement Δ_y was defined based on the criteria for equivalent elastic-plastic energy absorption. The peak displacement Δ_u referring to the peak load P_u was the maximum lateral load. The failure load P_f was defined as the post-peak displacement corresponding to 85% of the peak strength.

The hysteretic responses of torsion-twist and load-displacement for the specimens are shown in Figure 7a,b, respectively. The following observations could be summarized:

(1) Both the two hysteretic curves of the torsion-twist and the load-displacement exhibited an "S" shape. Due to the asymmetry of section, the asymmetry of the hysteresis curves were observed. Before cracking, the specimen exhibited elastic behavior and the hysteresis curve was narrow with little residual deformation after unloading. After cracking, a drop of secant stiffness was observed and the envelope area increased. After the peak load, the slope of secant stiffness dropped rapidly.

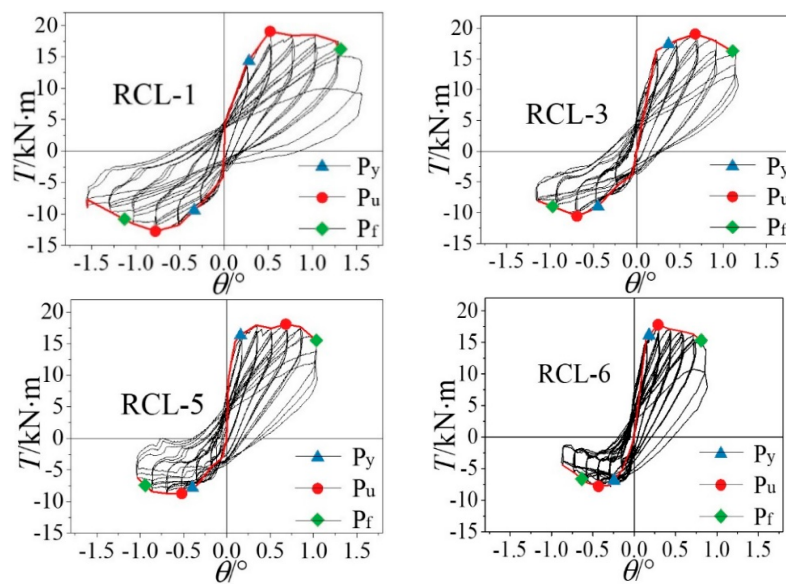
(2) Comparing with RCL-1 ($T/M = 0.36$), RCL-5 ($T/M = 0.28$), and RCL-6 ($T/M = 0.17$), it was noted that T/M ratio had a significant effect on the hysteretic behavior. For the relationship of torsion-twist, the slope of unloading stiffness and the degree of pinching increased with the increase of T/M ratio. This was attributed to the increase of T/M ratio that change the failure mode from the bending failure to torsion-shear failure. Therefore, the stiffness dropped rapidly and the pinching in the loops was relatively high. The plastic deformation of concrete also increases the ultimate rotation angle and hysteretic curve area. For hysteretic curves of lateral load-displacement, with the increase of T/M ratio, ultimate bearing capacity and ductility decrease. In addition, the hysteretic loops of the RCL-2 ($T/M = 0$) was plumper than these specimens under combined loading including torsion. It is indicated that the torsion had an adverse effect on seismic performance.

(3) Axial compression ratio was another important effect on hysteretic behavior. In particular, with the decrease of the axial compression ratio, the twist increased and the flexural capacity reduced while the bending energy consumption and ductility increase slightly.

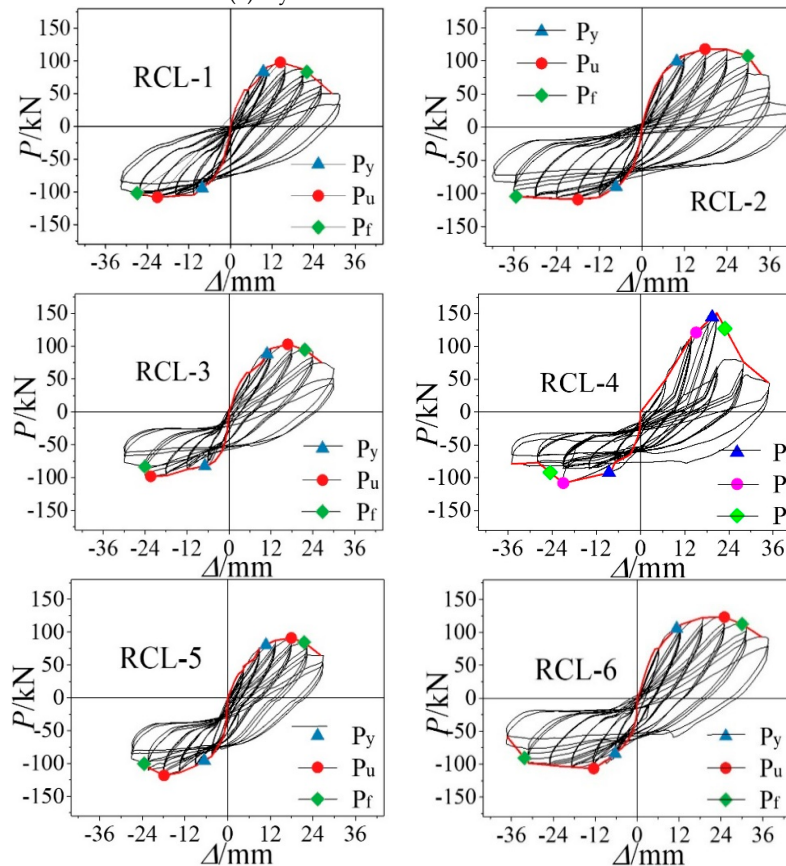
Table 2. Characteristics point of specimens.

No.	Loading Direction	Yield Point				Peak Point				Ultimate Point				$\gamma_{cr}/\%$	$\gamma_u/\%$	$\mu_\theta = \theta_u/\theta$	$\mu_\Delta = \Delta_u/\Delta_y$
		T_y	θ_y	P_y	Δ_y	T_m	θ_m	P_m	Δ_m	T_u	θ_u	P_u	Δ_u				
RCL-1	Push	14.3	0.28	83	9.5	19.1	0.52	98	14.4	16.2	1.32	83	22.0	1/316	1/54	4.84	2.31
	Pull	9.4	0.34	95	8.2	12.7	0.78	108	21.0	10.8	1.13	102	26.9	1/291	1/46	3.35	3.30
	Average	11.9	0.31	89	8.9	15.9	0.65	103	17.6	13.5	1.23	93	24.5	1/333	1/50	4.10	2.81
RCL-2	Push			99	9.8			117	17.8			107	29.8	1/388	1/39		3.03
	Pull			90	7.3			109	18.0			105	35.4	1/231	1/33		4.87
	Average			95	8.6			114	17.9			106	32.6	1/290	1/36		3.95
RCL-3	Push	17.4	0.37	88	10.9	19.1	0.68	103	16.8	16.3	1.11	95	21.7	1/266	1/39	6.69	1.99
	Pull	9.4	0.50	82	6.9	10.5	0.69	98	22.4	8.9	1.00	83	24.0	1/674	1/33	5.15	3.47
	Average	14.1	0.44	85	8.9	15.3	0.69	101	19.6	12.6	1.06	89	22.9	1/381	1/36	11.84	2.73
RCL-4	Push			165	16.1			176	20.7			159	25.5	1/316	1/53		1.38
	Pull			135	11.3			161	21.0			121	24.7	1/469	1/50		2.18
	Average			150	13.7			168	20.9			140	25.1	1/377	1/51		1.78
RCL-5	Push	15.8	0.20	80	10.8	17.0	0.68	91	17.9	14.5	0.97	85	21.6	1/490	1/52	4.86	1.99
	Pull	6.9	0.35	95	6.5	8.0	0.35	118	18.0	6.8	0.91	100	23.5	1/1008	1/49	2.57	3.60
	Average	11.4	0.28	88	8.7	12.5	0.52	105	18.0	10.7	0.94	93	22.6	1/659	1/51	3.72	2.80
RCL-6	Push	15.4	0.20	106	11.3	17.8	0.29	123	25.0	15.0	0.81	112	30.0	1/153	1/37	4.02	2.66
	Pull	6.4	0.22	84	6.3	7.8	0.43	107	12.4	6.6	0.63	91	32.2	-1/532	1/42	2.93	5.10
	Average	10.9	0.21	95	8.8	12.8	0.36	115	18.7	10.8	0.72	102	31.1	1/238	1/40	3.48	3.88

Note: The unit of torsion moment (T) is (kN·m); the unit of twist (θ) is ($^\circ$); the unit of lateral force (P) is (kN); the unit of lateral displacement (Δ) is (mm); the unit ductility factor (μ_θ and μ_Δ) is non-dimensional.



(a) Hysteretic curves of torsion-twist



(b) Hysteretic curves of the lateral load-displacement

Figure 7. Hysteretic curves of the torsion-twist and load-displacement.

4.2. Skeleton Curves and Characteristic Points

The skeleton curves of the torsion-twist and load-displacement for these specimens are depicted in Figure 8. The characteristic points (namely, the yielding lateral load P_y and yielding displacement Δ_y , the yielding torsion T_y and yielding twist angle θ_y , peak later load P_m and peak displacement Δ_m , peak torsion T_m and peak twist angle θ_y , ultimate lateral load P_u and ultimate displacement Δ_u , ultimate torsion T_u and ultimate twist angle θ_u) of the specimens, which were defined on the skeleton

curve, are listed in Table 2. In the following part, all the comparison of the characteristic value from Table 2 referred to the average value.

(1) The skeleton curves were similar in shape. All the skeleton curves consisted of linear elastic stage, elastic-plastic stage, and descending stage.

(2) It is noted that the specimen with bending failure exhibited a high bearing capacity and ductility. Besides, with the increase of T/M ratio, the skeleton curve dropped gently in the descending stage.

(3) For RCL-1 ($T/M = 0.36$), RCL-5 ($T/M = 0.28$) and RCL-6 ($T/M = 0.17$), with a decline in the T/M ratio, the yield torsion of RCL-5 and RCL-6 decreased by 4.5% and 9.1%, respectively, compared to the RCL-1, while the peak torsion decreased by 27.4% and 24.1%. It is indicated that with the increasing T/M ratio the torsion capacity increased significantly.

(4) Comparing to the specimen RCL-3 ($n = 0.19$), a reduction of 22.3% in ultimate torsion was observed for the specimen RCL-5 ($n = 0.23$). It was indicated that torsion capacity increased with the decline of the axial compression ratio.

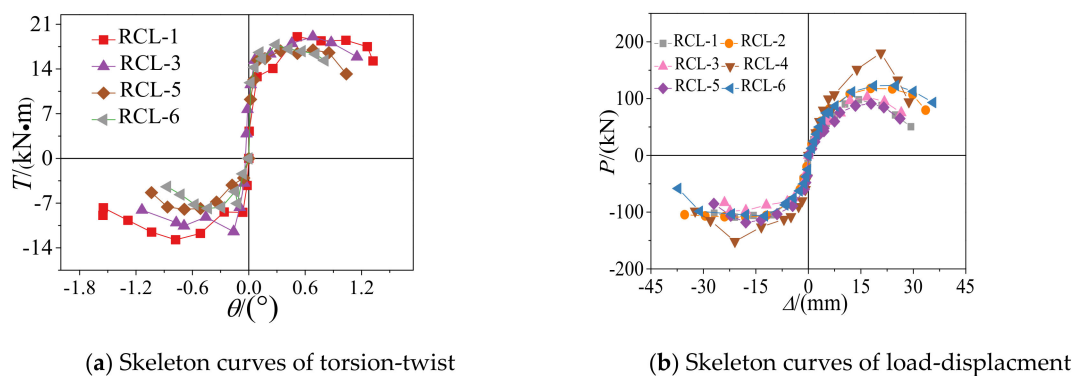


Figure 8. Skeleton curves for the specimens.

4.3. Deformation Capacity

Ductility factor (μ) is defined as the ratio of ultimate displacement to yield displacement (i.e., $\mu_{\Delta} = \Delta_u/\Delta_y$, $\mu_{\theta} = \theta_u/\theta_y$). Inter-story drift ratio γ is the ratio of lateral displacement to specimen length (i.e. $\gamma_{cr} = \Delta_{cr}/H$, $\gamma_u = \Delta_u/H$). The values of μ and γ were listed in Table 2.

(1) With the increase of the T/M ratio the twist ductility coefficient increased, while the trend is the opposite with the increase of the axial compression ratio. Specifically, With the increasing T/M ratio (0.17, 0.28, 0.36), the average twist ductility for the specimen RCL-5 and RCL-6 increased by 10.5% and 17.8%, respectively, compared to the specimen RCL-1 with T/M ratio of 0.17. While, the reduction of 32.1% in the twist ductility coefficient for the RCL-3 ($n = 0.19$) was observed compared to the RCL-5 ($n = 0.23$).

(2) For the displacement ductility, it decreases with the increase of T/M ratio. It was attributed to the high T/M ratio result in low plastic zone height. The specimens with T/M ratio of 0.36 and 0.17, respectively, attained 73.4% and 71.1% of the displacement ductility factor for the specimen with T/M ratio of 0.

(3) The limit of elastic story drift ratio and elastoplastic story drift ratio for the CFST frame structure in design code GB50936-2014 (2014) were 0.18% and 2.00%. The average value of the elastic story drift ratio for all specimens is 0.36% and the average value of the ultimate story drift ratio is 2.81%. It is indicated that the RC L-shaped column met the requirement of the standard in regions of high seismic intensity.

4.4. Energy Dissipation

In the seismic analysis, the equivalent damping coefficient (h_e) and energy dissipation was used to evaluate the energy dissipation capacity. The equivalent viscous damping coefficient could be calculated as Equation (4).

$$h_e = \frac{1}{2\pi} \frac{S_{(ABC+CDA)}}{S_{(\Delta OBE+\Delta ODF)}} \tag{4}$$

where $S_{(ABC+CDA)}$ = the area enclosed by a complete load cycle; $S_{(\Delta OBE+\Delta ODF)}$ = idealized energy dissipation assuming elastoplastic behavior, as shown in Figure 9. The equivalent viscous damping coefficients for all the specimens were listed in Table 3 and Figure 10. Energy dissipation were calculated based on hysteresis curves of the specimens and the result is illustrated in Figure 11.

(1) From Figure 10, it is observed that the axial compression increased the bending energy dissipation significantly. At the final loading stage, the bending energy dissipation capacity of specimen RCL-4 ($n = 0.28$) is about 11% higher than that of specimen RCL-2 ($n = 0.23$), while the bending energy dissipation capacity of specimen RCL-5 ($n = 0.23$) is around 14.5% higher than that of specimen RCL-3 ($n = 0.19$). For the torsion energy dissipation capacity, with the axial compression ratio increased the torsion energy dissipation capacity declined. In the failure stage, the specimen RCL-3 ($n = 0.19$) resulted in a 6.1% higher energy dissipation as compared to the specimen RCL-5 ($n = 0.23$).

(2) With the increase of displacement, the torsion energy-dissipated capacity keeps increasing although there is a slight fluctuation. This is attributed to the initial energy-dissipation capacity offered by outer concrete, which deactivated after the cracks appeared. The energy-dissipation capacity was offered by reinforcement skeleton and core concrete, resulting in the energy-dissipation capacity continues to grow after a slight fluctuation. The bending energy consumption increased slowly at the early stage and increased rapidly at the final stage, which is due to the increase of plastic displacement and the decreases of stiffness.

(3) The proportion of torsion energy dissipation was larger than bending energy dissipation until $5\Delta_y$. When the RC L-shaped column failed, the bending equivalent damping coefficient was about 0.08~0.28 and the torsion equivalent damping coefficient was about 0.13~0.23.

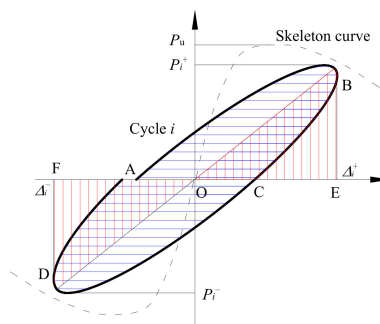


Figure 9. Diagram of energy dissipation.

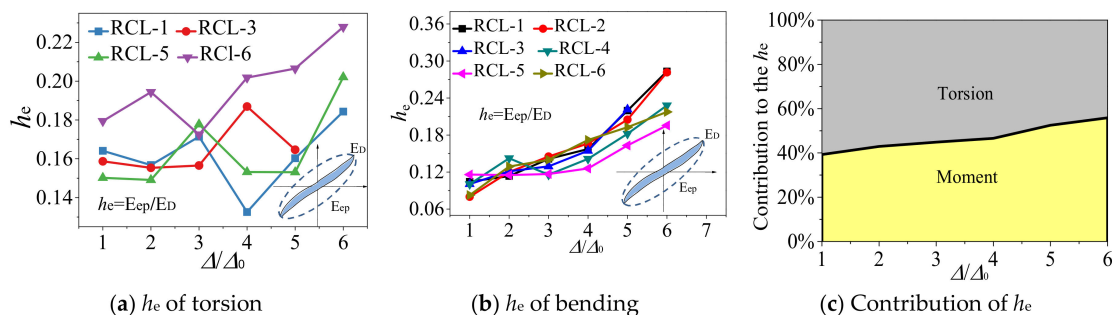


Figure 10. Equivalent damping ratio curves

Table 3. Equivalent damping ratio of specimens.

Specimen No.	Energy Dissipation	1 Δ_y	2 Δ_y	3 Δ_y	4 Δ_y	5 Δ_y	6 Δ_y
RCL-1	Bending	0.104	0.113	0.141	0.157	0.220	0.283
	Torsion	0.132	0.137	0.155	0.144	0.142	0.170
RCL-2	Bending	0.080	0.120	0.145	0.166	0.205	0.282
	Torsion	–	–	–	–	–	–
RCL-3	Bending	0.101	0.121	0.129	0.155	0.222	–
	Torsion	0.151	0.142	0.149	0.169	0.165	–
RCL-4	Bending	0.100	0.142	0.116	0.141	0.182	0.228
	Torsion	–	–	–	–	–	–
RCL-5	Bending	0.116	0.115	0.117	0.126	0.163	0.196
	Torsion	0.144	0.147	0.152	0.148	0.152	0.202
RCL-6	Bending	0.083	0.129	0.140	0.172	0.193	0.218
	Torsion	0.168	0.210	0.173	0.202	0.206	0.228

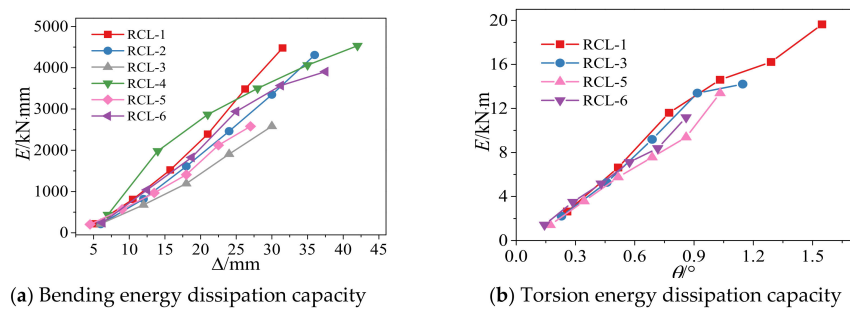


Figure 11. Bending and torsion energy dissipation capacity of specimens.

4.5. Stiffness and Strength Degradation

Secant stiffness (K) was used to evaluate the stiffness degradation under different displacement and twist levels, while strength degradation coefficient (λ) was used to evaluate the degree in different cycles under the same displacement and twist level. To better observe the trend of stiffness degeneration, the torsion stiffness and bending stiffness degradation curves are shown in Figure 12. The degradation curves of the torsion strength and bending strength are shown in Figure 13.

(1) Due to the formation of new cracks and yielding of reinforcements, the initial torsion stiffness degradation rate was high. Specifically, the torsion stiffness degraded by 50% when the displacement reached 3 Δ_y . After that, the rate of torsion stiffness degradation slowed down. Comparing with the RCL-1, RCL-5, and RCL-6, the initial stiffness and stiffness degradation decreased with the increase of T/M ratio. Due to the existence of torsion, the diagonal cracks extended to the whole specimen, which led to smaller torsion stiffness.

(2) The degradation of bending stiffness was more stable than torsion stiffness. The higher n ratio, the larger the bending stiffness, while the higher the T/M ratio, the less the bending stiffness.

(3) As shown in Figure 13, with the increase of axial compression ratio, the torsion strength degeneration coefficient increased due to the high compression, which could prevent the development of cracks.

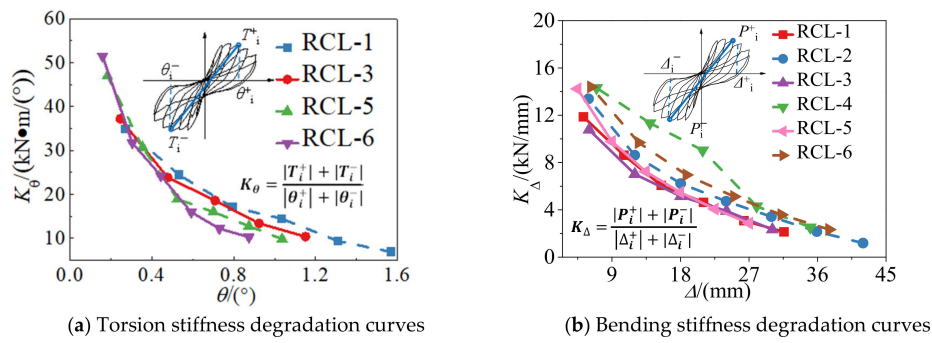


Figure 12. Stiffness degradation curves.

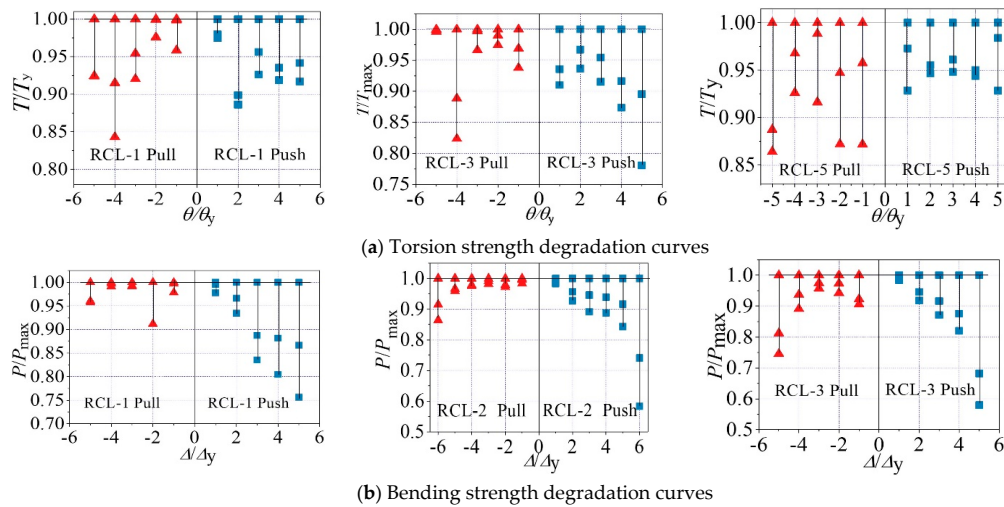


Figure 13. Strength degradation curves.

5. Proposed Modified Damage Index Mode

Combined loadings including torsion with axial compression, bending, and shear are commonly observed during the earthquake. Especially, the effect of combined loadings is significant to the special-shaped column frame. The adverse effect resulted in complex flexural-shear failure. Based on the finding of experiment, the torsion could reduce the length of plastic hinge and change the failure mode. In addition, the experiment showed that with the increase of torsion a reduction of flexural strength was observed. Therefore, it is necessary to quantify the damage degree of the RC special-shaped column under combined loadings resulting from the seismic load.

In this study, the damage index of flexure and torsion were obtained directly from the experimental hysteresis data. The Kumar damage model [30] was modified to predict the damage process of the special-shaped column under the combined loading including torsion. The model was decoupled to distinguish the influence of bending and torsion from the bending-shear-torsion loading state.

5.1. Flexural Damage Index Using the Kumar Approach

The Kumar model is the most widely used damage index for the RC column to quantify the damage as follows in Equation (5) [31–33].

$$D = (1 - \beta) \sum_{j=1}^{N_i} \left(\frac{\Delta_{\max,j} - \Delta_y}{\Delta_{u,i} - \Delta_y} \right)^c + \beta \sum_{j=1}^{N_i} \left(\frac{E_i}{E_{u,i}} \right)^c \tag{5}$$

where Δ_i = maximum displacement in the i th half-cycle; Δ_{\max} = maximum displacement experienced so far; E_i = hysteretic energy dissipated in the i th half-cycle; β = damage parametric constant.

C = damage parametric constant, which could be calculated by the equation proposed by Wang [34].
 $c = 5.69 + 0.87 \ln^{\rho v} + 0.056 \lambda + 10.46 \rho_s - 2.1n$.

In this study, the Kumar approach was modified by the experimental result to quantify the flexural damage under the combined loading. The flexural damage index parameters β could be obtained through the multiple nonlinear regression analysis as shown in Figure 14 and the expression of the damage index parameters β was shown in the Equation (6)

$$\beta_{flexural} = 0.5887n - 2.2896\gamma^2 + 0.8934\gamma - 0.0649 \tag{6}$$

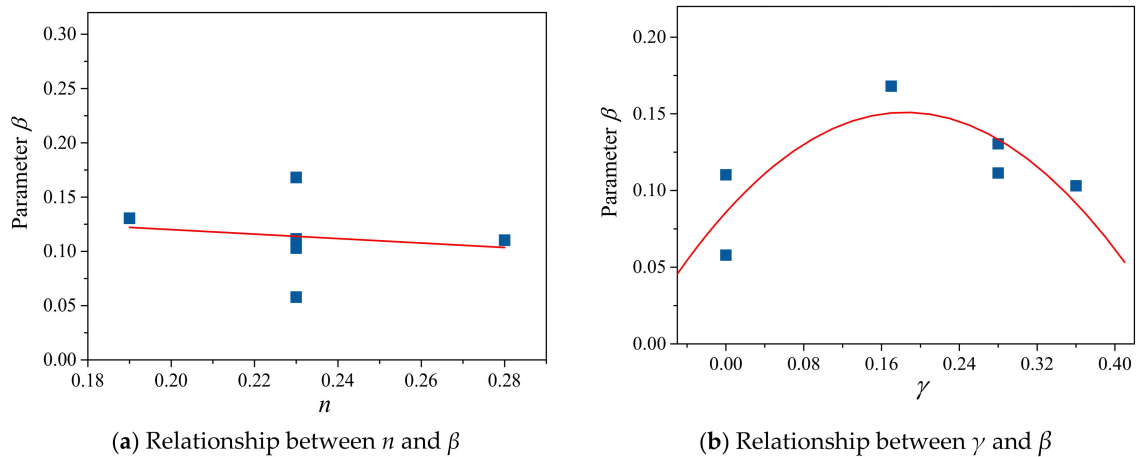


Figure 14. Relationship curves of flexural damage parameter β .

5.2. Torsional Damage Index Using the Kumar Approach

The Kumar model was also modified and extended to predict the progression of the torsion damage state under the combined loading. The following equation (6) was proposed for the torsional damage parameter β through the nonlinear regression analysis. The process of nonlinear regression is shown in Figure 15.

$$\beta_{torsional} = -0.6035n - 0.0246 \ln(\gamma) + 0.1484 \tag{7}$$

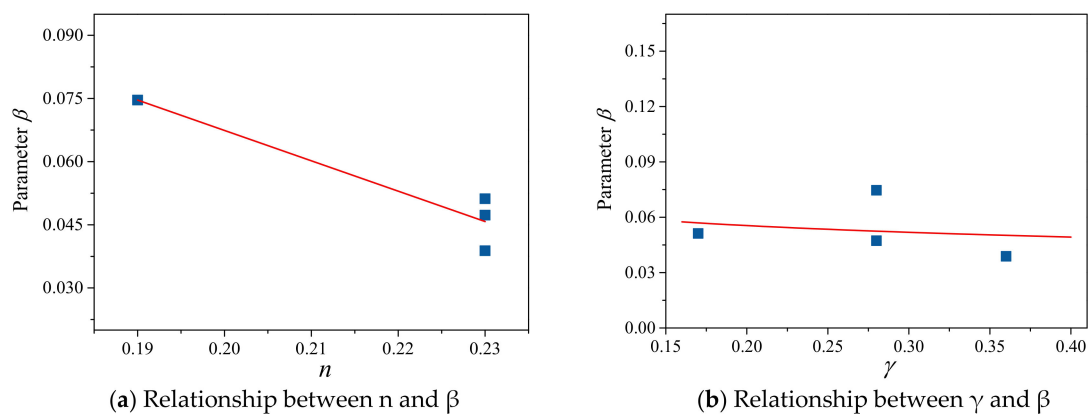


Figure 15. Relationship curves of torsional damage parameter β .

5.3. Unified Equivalent Damage Index

During the loading process, the torsion and flexure act together on the column. Hence, the torsional and flexural damage indices should be combined to evaluate the damage process. Accounting for the approach proposed by the Li [21], the weight coefficient of T/M ratio was applied in calculating

the Unified Equivalent Damage Index. The Unified Equivalent Damage Index (UEDI) was calculated by Equation (8)

$$UEDI = m \times FDI + t \times TDI$$

$$m = \frac{1}{1+T/M}$$

$$t = 1 - m$$
(8)

where m is weight ratio of bending moment; t is weight ratio of torsion moment; FDI is the decoupled flexural damage index under combined loading; TDI is the decoupled torsional damage index under combined loading.

The Unified Equivalent Damage Index increased with the ductility level up to the failure as shown in Figure 16. As depicted in figure, the increasing T/M ratio raised the value of the UEDI for the specimens under combined loadings.

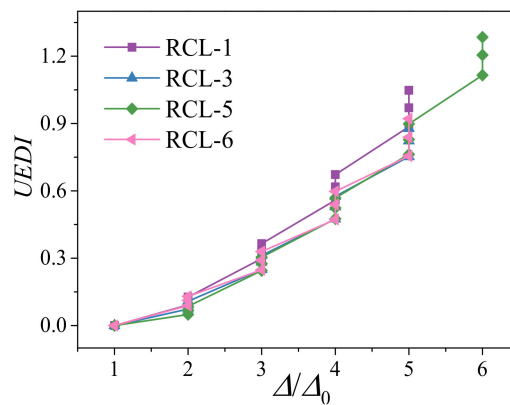


Figure 16. Unified Equivalent Damage Index under Combined Loadings.

5.4. Influence of Torsion on Damage Index

The two types of damage index were calculated to the failure state according to the two proposed damage model. The influence of T/M ratio on the progression of damage state predicted by the proposed model is clearly shown in Figure 17. It was observed that the damage index was rising with the increase of the ductility level and the damage value was a little higher than one when reached the failure state. Besides, in the same ductility level the damage index value increase with increasing loading cycles, which is in accord with the progression of damage.

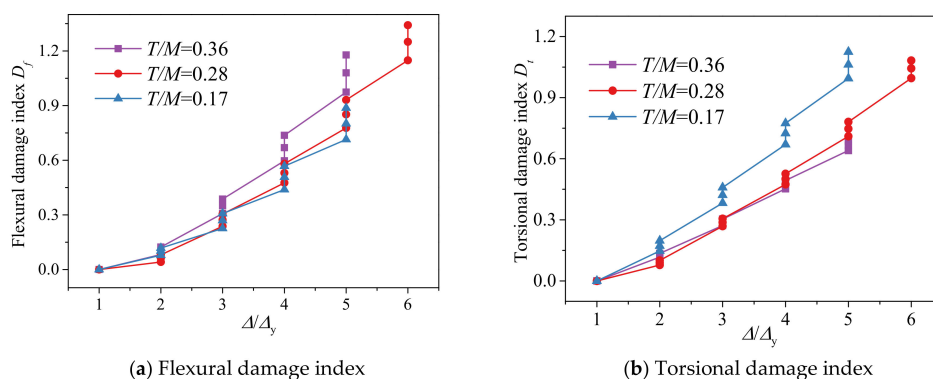


Figure 17. Influence of T/M ratio on the damage index.

The flexural damage curve obtained a steeper slope compared to the specimen with the lower T/M ratio. It may be attributed to the smaller length of plastic hinge result from the effect of the torsion. Therefore, the displacement ductility dropped with the increasing T/M ratio. The torsion damage index

value decline when the T/M ratio increase. As the increase of the T/M ratio led to the change of failure mode from the flexural failure to the torsional failure, the torsional rotation ductility improved.

5.5. Influence of Axial Compression Ratio on Damage Index

The influence of axial compression ratio on the progression of damage state predicted by the proposed model is clearly shown in Figure 18. The flexural damage curve with the greater axial compression ratio obtained a higher damage index compare to the lower axial compressive ratio. This may attribute to the better ductility due to the lower axial compression ratio. In the same ductility level, the better ductility resulted in a lower damage index. For the torsional damage model, the lower axial compression ratio obtained a steeper slope of the damage curve. Since the stronger confinement was caused by the higher compression, the cracking of concrete delayed which improved the torsional rotation ductility. It is indicated that the progression of torsional damage is quietened by high compression.

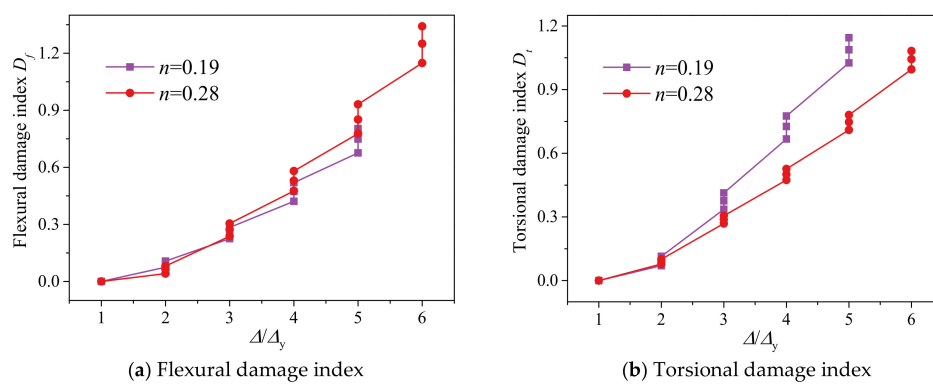


Figure 18. Influence of axial compression ratio on the damage index.

6. Conclusions

This paper presents the results of tests on reinforced concrete L-shaped columns under combined constant axial loading and cyclic flexure-shear-torsion loading. The effects of ratio of torsion-moment (T/M) and axial compression ratios (n) on bearing capacity, ductility, inter-story drift ratio, energy dissipation, stiffness degradation, and strength degradation were discussed. These experimental results and comparisons were summarized as follows:

(1) With the variation of the T/M ratios, the failure modes of reinforced concrete L-shaped columns included bending failure, flexure-torsion failure, and torsion-shear failure. With the increase of T/M ratio, the cracks propagated upward and the height of concrete crushed area decreased. The cracks were mainly concentrated on the column limb parallel to loading direction.

(2) All the hysteretic loops exhibited pinched "S" shape. Under the same T/M ratio, the hysteretic loops of the load-displacement were plumper than the hysteretic loops of torsion-twist. With the increasing of T/M ratio, the hysteretic loops had a more obvious pinching phenomenon.

(3) With the increase in T/M ratio, the torsion bearing capacity and torsion ductility factor increase significantly, while the bending bearing capacity and displacement ductility factor decreased. With the increasing axial compression ratio, the reductions of torsion and bending bearing capacity were observed.

(4) The total energy dissipation in early stage was mainly caused by torsion while in the failure stage was governed by flexure. The bending and torsion equivalent damping coefficient for the failure point was about 0.2~0.28 and 0.16~0.23, respectively. The rate of stiffness degradation for bending as lower than that of torsion while the rate of strength degradation is opposite. The average value of the story drift ratio is over 2.81% indicating a favorable anti-collapse performance for the L-shaped RC column.

(5) Two modified damage index models were proposed to clearly predict the progression of damage for the special-shaped column under combined loading. Decreasing T/M ratio helped to prevent the flexural damage of specimen and a low T/M ratio lead to the critical torsional damage of the specimen. An increase in axial compression ratio resulted in more confinement for the cracking, thus reducing the torsional damage. While, with the axial compression ratio increase, the flexural damage index value increase.

Author Contributions: Conceptualization, Z.C.; Formal analysis, D.X.; Funding acquisition, Z.C.; Methodology, D.X.; Writing—original draft, D.X.; Writing—review and editing, Y.Y. and Z.C. All authors have read and agreed to the published version of the manuscript.

Funding: The research reported in this manuscript was supported by the National Natural Science Foundation of China (N0.51268004 and 51578163), and Key Project Natural Science Foundation of Guangxi (No: 2016GXNSFDA380032).

Acknowledgments: The writers also appreciate the assistance that was provided by Xiang Liu and Yang Yang during the experimental process.

Conflicts of Interest: The authors declare no conflict of interest.

References

1. Wu, H.; Qiao, Q.; Cao, W.; Dong, H.; Zhang, J. Axial compressive behavior of special-shaped concrete filled tube mega column coupled with multiple cavities. *Steel Compos. Struct.* **2017**, *23*, 633–646.
2. Rong, B.; Feng, C.; Zhang, R.; You, G.; Liu, R. Compression-bending performance of L-shaped column composed of concrete filled square steel tubes under eccentric compression. *Int. J. Steel Struct.* **2017**, *17*, 325–337. [[CrossRef](#)]
3. Mahadevappa, P. Computer aided analysis of reinforced concrete columns subjected to axial compression and bending—I L-shaped sections. *Comput. Struct.* **1992**, *44*, 1121–1138.
4. Sinha, S.N. Design of cross (+) section of column. *Indian Concr. J.* **1996**, *70*, 153–158.
5. Rahaman, A.; Anik, A.M.; Serker, N.H.M.K. Effect of Special Shaped Column on Lateral Load Resistance Capacity of Reinforced Concrete (RC) Building. *Am. J. Civ. Eng.* **2018**, *6*, 147–153. [[CrossRef](#)]
6. Raj, A.B.; Kumar, D.R. Buckling Behaviour and Lateral Load Performance of Web Tapered Sectional Steel Columns. *Int. Res. J. Adv. Eng. Sci.* **2019**, *4*, 363–367.
7. Dahiya, N.; Sehgal, K.V.; Saini, B. Analysis and design of rectangular and L-shaped columns subjected to axial load and biaxial bending. *Int. J. Struct. Eng. Anal.* **2016**, *2*, 15–22.
8. Al-Ansari, M.S.; Afzal, M.S. Simplified irregular column analysis by equivalent square method. *J. Struct. Eng.* **2019**, *2*, 36–46. [[CrossRef](#)]
9. Zhou, T.; Xu, M.Y.; Chen, Z.H.; Wang, X.; Wang, Y.W. Eccentric loading behavior of L-shaped columns composed of concrete-filled steel tubes. *J. Adv. Steel Construct.* **2016**, *12*, 227–244.
10. Cao, W.; Hu, G.; Cui, L.; Zhou, M.; Hao, C.; Qu, Y. Experiment and analysis of seismic behavior of the +, L, T-shaped columns with concrete columns. *J. Build. Struct.* **2002**, *1*, 16–20, 26.
11. Liu, J.; Lu, Z.; Feng, J. Study on Shaking Table Test of a 9-storey RC Frame Model with Specially Shaped Columns and Transfer Storey. *J. Buil. Struct.* **2002**, *1*, 21–26.
12. Cui, Q.; Yang, J.; Kang, G. Experimental research on seismic behavior of Z-shaped column joints in RC frame. *J. Buil. Struct.* **2012**, *6*, 86–95.
13. Li, B.; Pham, T.P. Experimental Study on the Seismic Response of L-Shaped Reinforced Concrete Columns. In *Structures Congress: Bridging Your Passion with Your Profession 2013*; ASCE: Reston, VI, USA, 2013; pp. 1673–1682.
14. Nie, J.-G.; Wang, Y.-H.; Fan, J.-S. Experimental study on seismic behavior of concrete filled steel tube columns under pure torsion and compression–torsion cyclic load. *J. Construct. Steel Res.* **2012**, *79*, 115–126. [[CrossRef](#)]
15. Nie, J.-G.; Wang, Y.-H.; Fan, J.-S. Experimental research on concrete filled steel tube columns under combined compression-bending-torsion cyclic load. *Thin-Walled Struct.* **2013**, *67*, 1–14. [[CrossRef](#)]
16. Otsuka, H.; Takeshita, E.; Urakawa, Y. Seismic performance and correlation characteristics of reinforced concrete columns subjected to torsional moment, bending moment/shear force and axial force. *Doboku Gakkai Ronbunshu* **2005**, *81*, 123–139. [[CrossRef](#)]

17. Hsu, H.L.; Wang, C.L. Flexural–torsional behaviour of steel reinforced concrete members subjected to repeated loading. *J. Earthq. Eng. Struct. Dyn.* **2000**, *29*, 667–682. [[CrossRef](#)]
18. Hsu, H.-L.; Hsieh, J.-C.; Juang, J.-L. Seismic performance of steel-encased composite members with strengthening cross-inclined bars. *J. Construct. Steel Res.* **2004**, *60*, 1663–1679. [[CrossRef](#)]
19. Tirasit, P.; Kawashima, K. Seismic performance of square reinforced concrete columns under combined cyclic flexural and torsional loadings. *J. Earthq. Eng.* **2007**, *11*, 425–452. [[CrossRef](#)]
20. Li, Q.; Belarbi, A. Performance based design approach for RC square bridge columns under combined loadings including torsion. *Struct. Congr.* **2012**, *2012*, 2223–2234.
21. Li, Q.; Belarbi, A. Damage assessment of square RC bridge columns subjected to torsion combined with axial compression, flexure, and shear. *KSCE J. Civil Eng.* **2013**, *17*, 530–539. [[CrossRef](#)]
22. Belarbi, A.; Ayoub, A.; Greene, G.; Prakash, S.; Mullapudi, R. Seismic performance of reinforced concrete bridge columns subjected to combined loading including torsion. In *Structural Engineering Research Frontiers*; ASCE: Reston, VI, USA, 2007; pp. 1–16.
23. Prakash, S.; Belarbi, A.; You, Y.-M. Seismic performance of circular RC columns subjected to axial force, bending, and torsion with low and moderate shear. *Eng. Struct.* **2010**, *32*, 46–59. [[CrossRef](#)]
24. Wang, P.; Han, Q.; Du, X. Seismic performance of circular RC bridge columns with flexure–torsion interaction. *Soil Dyn. Earthq. Eng.* **2014**, *66*, 13–30.
25. Deng, J.; Ma, Z.J.; Liu, A.; Cao, S.; Zhang, B. Seismic performance of reinforced concrete bridge columns subjected to combined stresses of compression, bending, shear, and torsion. *J. Bridge Eng.* **2017**, *22*, 04017099. [[CrossRef](#)]
26. Anumolu, S.; Abdelkarim, O.I.; ElGawady, M.A. Behavior of hollow-core steel-concrete-steel columns subjected to torsion loading. *J. Bridge Eng.* **2016**, *21*, 04016070. [[CrossRef](#)]
27. Mullapudi, T.; Ayoub, A. Analysis of reinforced concrete columns subjected to combined axial, flexure, shear, and torsional loads. *J. Struct. Eng.* **2013**, *139*, 561–573. [[CrossRef](#)]
28. Prakash, S.S.; Belarbi, A. Towards damage-based design approach for RC bridge columns under combined loadings using damage index models. *J. Earthq. Eng.* **2010**, *14*, 363–389. [[CrossRef](#)]
29. Belarbi, A.; Prakash, S.; Silva, P. Incorporation of decoupled damage index models in the performance-based evaluation of RC circular and square bridge columns under combined loadings. *ACI Spec. Publ.* **2010**, 79–102. [[CrossRef](#)]
30. Kumar, S.; Usami, T. Damage evaluation in steel box columns by cyclic loading tests. *J. Struct. Eng.* **1996**, *122*, 626–634. [[CrossRef](#)]
31. Chen, S.; Xie, X.; Zhuge, H.J.E.S. Hysteretic model for steel piers considering the local buckling of steel plates. *Eng. Struct.* **2019**, *183*, 303–318. [[CrossRef](#)]
32. Cai, J.; He, S.; Jiang, Z.; Chen, Q.; Zuo, Z.J.M. Structures, Experimental investigation on hysteretic behavior of thin-walled circular steel tubes under constant compression and biaxial bending. *Mater. Struct.* **2016**, *49*, 5285–5302. [[CrossRef](#)]
33. Cetinkaya, O.T.; Nakamura, S.; Takahashi, K. Ultimate strain of stiffened steel box sections under bending moment and axial force fluctuations. *Eng. Struct.* **2009**, *31*, 778–787. [[CrossRef](#)]
34. Wang, B. *Research on Seismic Damage of Steel Reinforced High Performance Concrete Members and Frame Structures*; College of Civil Engineering Xi'an University of Architecture & Technology: Xi'an, China, 2010. (In Chinese)

